REPORT CDOT-YYYY-XX

February 2023

Remote Monitoring of Avalanche Terrain with Terrestrial Laser Scanning and UAV

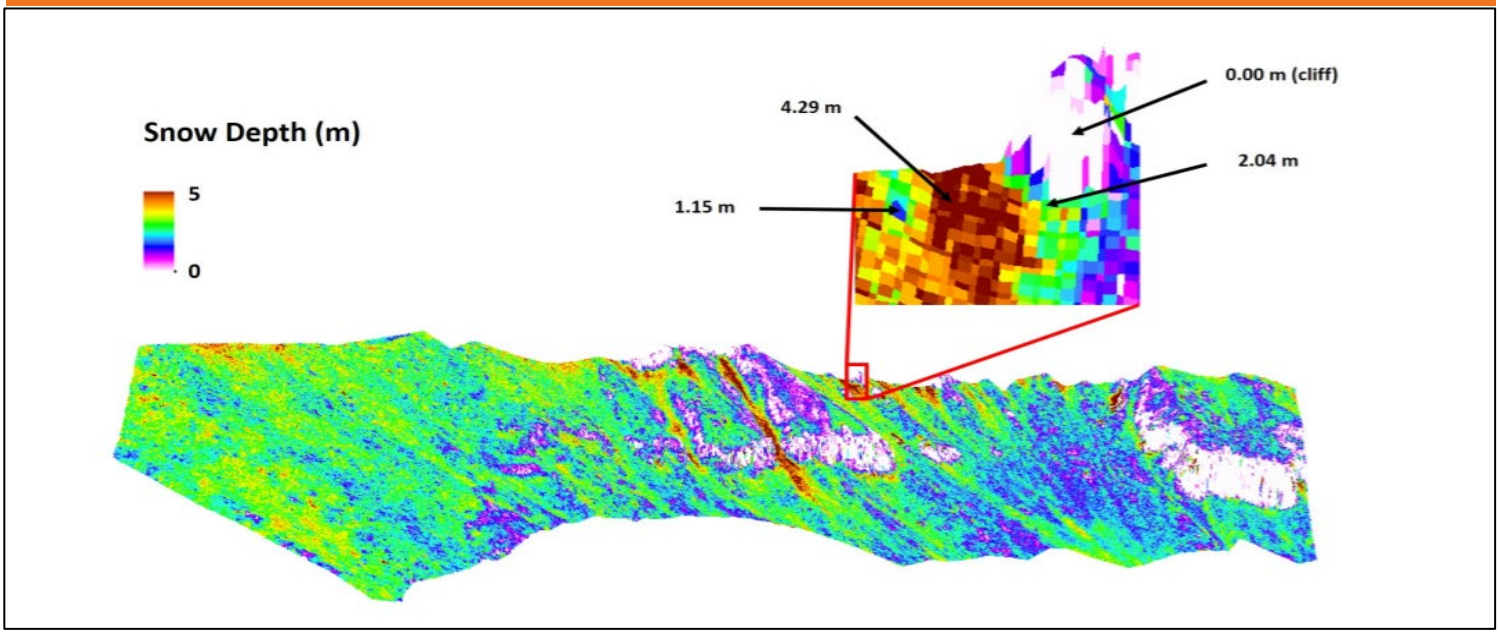

APPLIED RESEARCH & INNOVATION BRANCH

Dr. Kevin Hammonds

Dr. Thor Veen

Mr. Eelke Folmer

Mr. James Dillon

COLORADO
Department of Transportation

Technical Report Documentation Page

1. Report No.	2. Government Accession No.	3. Recipient's Catalog No.
CDOT-2023-XX		

4. Title and Subtitle	5. Report Date
Remote Monitoring of Avalanche Terrain with Terrestrial Laser Scanning and UAV	February 2023
	6. Performing Organization Code

7. Author(s)	8. Performing Organization Report No.
Kevin Hammonds, Thor Veen, Eelke Folmer, James Dillon	

9. Performing Organization Name and Address	10. Work Unit No. (TRAIS)
Montana State University 205 Cobleigh Hall Bozeman, MT 59717	11. Contract or Grant No. 5337.06

12. Sponsoring Agency Name and Address	13. Type of Report and Period Covered
Colorado Department of Transportation - Research 2829 W. Howard Pl. Denver CO, 80204	Final
	14. Sponsoring Agency Code

15. Supplementary Notes

Prepared in cooperation with the US Department of Transportation, Federal Highway Administration

16. Abstract

Remote sensing of avalanche terrain with Terrestrial Laser Scanning (TLS) and Un-crewed Aerial Vehicles (UAVs) can provide key insights to guide avalanche forecasting. Technological advances in remote sensing and data processing open new opportunities to collect data at previously impossible or prohibitively expensive spatial scales. Though utilized with increasing frequency in the cryosphere (e.g., fields of climatology and glaciology), the use of remote sensing systems for avalanche forecasting is in its infancy. Promising recent work has demonstrated the capacity of TLS to estimate snow depth on the basis of digital elevation model (DEM) differencing (i.e., winter DEM - summer DEM). This allows for spatially continuous and extensive data products, such as maps of overall snow depth or depth atop a known weak layer, across entire drainage basins at centimeter resolution. However, such data products require additional validation and streamlining, and it is unclear if other remote sensing systems can produce depth maps of comparable accuracy. Similarly, remote data products other than snow depth, such as snow density, have yet to be investigated. In this TARP-funded collaboration between MSU and Aeria (Phase 3 of original TARP award), we implemented a four-pronged approach toward operationalizing remote sensing for avalanche forecasting and control which included validation of data derived from TLS and UAV, creation of a user-friendly GIS interface for mapping snow depth, and in conducting controlled laboratory experiments to investigate relevant snow parameters for avalanche forecasting operations. This final report concludes the work of three ongoing years of research supported by the Transportation Avalanche Research Pooled Fund Program.

17. Keywords	18. Distribution Statement
Insert keywords	This document is available on CDOT's website https://www.codot.gov/programs/research

19. Security Classif. (of this report)	20. Security Classif. (of this page)	21. No. of Pages	22. Price
Unclassified	Unclassified		

Table of Contents

1. Introduction

The spatial distribution of physical snowpack parameters, such as snow depth and density, in avalanche start zones is a key determinant of avalanche formation and character. Substantial changes in snowpack properties over short spatial scales are not uncommon in mountainous environments, particularly in heavily wind-affected regions. Knowledge of differential loading and spatial distributions of various physical snowpack properties is a substantial advantage for avalanche forecasting and control practitioners. For example, it has been demonstrated that avalanche control efforts are often more successful when targeting shallow regions adjacent to deep slabs, leveraging observations of disparate snow depth over relatively short lengths. Unfortunately, traditional observations of snowpack properties often involve discrete, manual measurements, potentially exposing personnel to dangerous terrain hazards and yielding only spotty, spatially discontinuous datasets.

Remote sensing of avalanche terrain with Terrestrial Laser Scanning (TLS) and Un-crewed Aerial Vehicles (UAVs) can provide key insights to guide avalanche forecasting. Technological advances in remote sensing and data processing open new opportunities to collect data at previously impossible or prohibitively expensive spatial scales. Though utilized with increasing frequency in the cryosphere (e.g., fields of climatology and glaciology), the use of remote sensing systems for avalanche forecasting is in its infancy. Promising recent work has demonstrated the capacity of TLS to estimate snow depth on the basis of digital elevation model (DEM) differencing (i.e., winter DEM - summer DEM). This allows for spatially continuous and extensive data products, such as maps of overall snow depth or depth atop a known weak layer, across entire drainage basins at centimeter resolution. However, such data products require additional validation and streamlining, and it is unclear if other remote sensing systems can produce depth maps of comparable accuracy. Similarly, remote data products other than snow depth, such as snow density, have yet to be investigated.

In this TARP-funded collaboration between MSU and Aeria (Phase 3 of original TARP award), we implemented a four-pronged approach toward operationalizing remote sensing for avalanche forecasting and control. The goals of our project were as follows:

1) Further validate and optimize the use of TLS for snow depth mapping.
2) Evaluate the performance of UAV/photogrammetry for snow depth mapping against TLS, while documenting strengths and weaknesses.
3) Create a user-friendly GIS interface specifically for the purpose of mapping snow depth with remote sensing platforms.
4) Conduct a controlled laboratory experiment to investigate remote extraction of other snowpack parameters relevant to forecasting.

This document describes the methodology and current results regarding each objective.

2. Methodology

2.1 Field Study Areas

Data collection took place at four general locations with various subsites therein, spanning from 2020 to 2022. Two local ski resorts, the Yellowstone Club and Bridger Bowl Ski Area, were kind enough to facilitate several data outings, while TARP partners WSDOT and WYDOT provided access to Stevens Pass and Teton Pass, respectively. Data acquisition focused on depth mapping, validation measurements, and observations surrounding avalanche control efforts. The “West Camp” and “Old Faithful” sites were explored on Stevens Pass, while Glory

Bowl and Twin Slides were the focus of Teton Pass. Comparative collections between TLS and UAV-based photogrammetry took place between February 3 – 6, 2022, spanning Teton Pass, the Yellowstone Club, and Stevens Pass.

2.2 Lidar TLS

2.2.1 Instrument

For the analyses presented here, a Riegl VZ-6000 terrestrial laser scanner was used (Figure 1). The VZ-6000 is mounted to a tripod and achieves vertical (line) scanning via an oscillating mirror while moving horizontally on a rotating head; it is primarily designed for long-range field applications, with a maximum range in excess of 6 km. The maximum vertical scan field-of-view is 60° - 120° from zenith and selectable therein, while the horizontal field-of-view can range from 0° to a full 360° panorama. The laser operates in the NIR range narrowly around a central wavelength of 1064 nm. Vertical and horizontal angular increments are selectable and were frequently set to 0.01° to maximize resolution (point density). The initial laser beam diameter upon exiting the scanner is 15 mm with a divergence of 0.12 mrad. Individual scans typically take between 5 and 40 minutes, depending on the size of the scan area and the desired resolution, producing point clouds with upwards of 1 million points and typical spacing of 1 – 20 pts/m^2. Resulting point clouds were processed, including alignment and spatial referencing, in Riegl's proprietary Riscan software prior to exportation for analyses.

Figure 1. VZ-6000 collecting data near Pioneer Mountain at the Yellowstone Club.

2.2.2 Spatial Referencing and Validation

To achieve depth mapping, a snow-on DEM must be aligned with and compared to either a snow-off or an earlier snow-on DEM, depending on the desired snow depth product (Figure 2). Thus, rigorous spatial alignment is critical. This is often accomplished using tie point reflectors, typically in the form of mounted, circular metallic disks of prescribed diameter. Fine scans of these tie points are acquired during each outing, and coincident tie points between scans are used to align the point clouds as rigid bodies via translation/rotation. This process is termed relative alignment or referencing, as the clouds are simply aligned relative to one another. Alternately, if GPS points corresponding to the tie points are acquired (e.g., with the Emlid workflow to be described in Section 2.3.1), then point clouds can be globally georeferenced as well, allowing for compatibility with external datasets. In the absence of tie points, relative and global alignment can still be achieved; the Riegl Multi-Station Alignment

(MSA) workflow can be used to align clouds based on permanent structures, or even natural features. However, this is best left for relative alignment between lidar scans, as global correction of roll, pitch, and yaw is difficult to accomplish without adequate tie points.
Once scans have been aligned and depth maps calculated, lidar-based depth estimates were compared to manual observations, or ground truth. The most formal ground truthing primarily took place at Bridger Bowl Ski Area on eight outings during the 2020 – 2021 winter season. Six manual depth measurements were made per outing (48 points total), corresponding to visible indicators that could be located within the lidar scans to circumvent the need for GPS points and referencing. Observations were made on a test slope above the Alpine ski lift, the angle of which varied from 0 - 35°. The underlying ground surface was generally grassy with occasional rock outcrops. Error was evaluated both as an absolute metric and as a function of total snow depth.

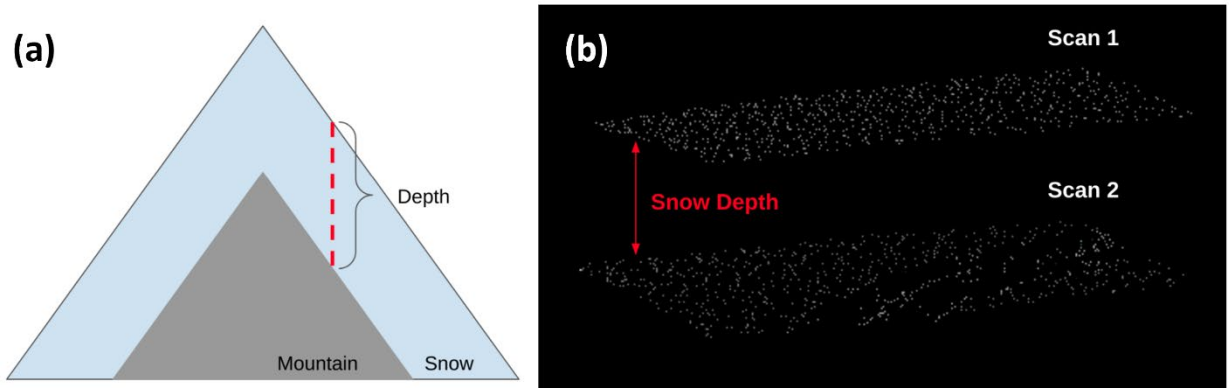

Figure 2. Schematic (a) and demonstration (b) of snow depth map calculation from point cloud/DEM differencing.

2.3 UAV Photogrammetry

2.3.1 Flight Parameters and Other Material

We selected a light-weight quadcopter Autel EVO 2 RTK UAV for aerial mapping for several reasons. It has ~30 minutes flight time and provides reliable and safe flights at low temperatures. Because of its relatively low weight and small size it is well suited for launching and landing in areas with limited space, such as mountain tops and roadsides. It is equipped with a high precision GNSS receiver and is RTK enabled which allows for cm-level positioning which is required for the construction of accurate maps by means of photogrammetry without the need for Ground Control Points (GCP). We worked with five spare batteries which were kept warm before being used.

Flight elevation was approximately 75m above ground level and the forward overlap 80% and side overlap 60%. The missions required 4-5 individual flights with 500-600 images per flight. We used UgCS software for mission planning as it allows terrain following based on an external elevation model. Flight speed was automatically calculated by UgCS.
In order to independently check the accuracy of the produced maps and to be able to compare the DEMs derived from the UAV with the one from the TLS we deployed GCPs at our survey sites. These are square 50 by 50 cm cloth sheets with black and white markings on them which are well visible in the aerial imagery. The location of these GCPs were recorded with an Emlid survey kit consisting of two RS2 GNSS receivers, one of which was used as a base station and one as a rover. The base station was screwed onto a solid tripod at a place with no disturbance and switched on at the start of the operation and switched off at the end of operation. The rover

was located on a survey pole set to 2 meters. All measurements were recorded with the Emlid ReachView 3 app with a recording time for each measurement of 10 seconds. Figure 3 shows an example of a UAV landing after conducting an automated mapping mission.

Figure 3. UAV and base station setup.

2.3.2 PPK processing and photogrammetry

We used a Post Processing Kinematics (PPK) geotagging workflow to obtain accurate locations of the cameras[1]. The input for PPK processing are the images from the UAV, the UAV RINEX file, the UAV trigger file which contains the filenames of the images and the timestamps, and the RINEX file from the base station. We used the REDToolBox software for geotagging. The output is a text file with accurate locations of the camera positions which is the input for photogrammetry.

We used Agisoft Metashape for photogrammetry. Agisoft Metashape is an advanced desktop program which provides a lot of control to the user. Photogrammetry of snow-covered surfaces is challenging mainly due to the homogeneous surfaces in which few tie points can be identified. The manual control that Agisoft Metashape allows during the photogrammetry workflow provides important benefits in such cases. We refer to the Agisoft Metashape user manual for an excellent description of the photogrammetry workflow.

2.3.3 Ground Control Points

EMLID RS2s are used as a base station and rover to survey the location of reference points (e.g. GCP). To obtain absolute cm-level accuracy precise point positioning (PPP) is required which is provided by NRCAN[2] free of charge. As mentioned above, we used

[1] Camera in this context means the xyz location of the sensor of the UAV at the time the images are taken.

[2] The positions are based on the NAD83(CSRS) datum and the 2022.1 epoch. NAD83(CSRS) is a re-adjustment of the original NAD83 datum. Because of tectonic movement positions on earth surface move in relation to the datum. For that purpose, it is necessary to define a reference

REDToolBox for PPK geotagging of the images before photogrammetry. Just like the UAV, the Emlid rover measures its location in relation to the base station. They both use a-priori positions of the base station. However, the a-priori position of the base station used by the Emlid rover is different from the calculated position of the UAV as used by REDToolBox (the input here is the entire RINEX file). Hence, before matching the GCP coordinates with the orthomosaic, the GCP coordinates are shifted on the basis of the difference between the coordinates of the a-priori base station and the RINEX header.

2.3.4 Spatial referencing

For validation of the accuracy of orthomaps and digital elevation models it is important that the data are in the same coordinate reference system. We check the accuracy of the maps by comparing the location (xyz coordinates) of ground control points in the in the orthomosaics with independently measured xyz location using RTK enabled GNSS system. The vertical accuracy of the DEM is checked by comparing the DEM-elevation with the ellipsoid height of the GCP. The data are compared in the geographic coordinate reference system World Geodetic System (WGS84) which is a standard for use in cartography, geodesy and satellite navigation. Furthermore, photogrammetry-based DEMs were compared to those produced by the TLS from corresponding outings.

2.4 Software Development

Though numerous proprietary and open-source Geographic Information Systems (GISs) are capable of processing point cloud data from various remote sensors, this requires a certain level of GIS expertise. To reduce this barrier and streamline the use of TLS and photogrammetry-based data for forecasting analytics, we have created an open-source GIS software product tailored to the avalanche community (Figure 4). Our goal was to create a user-friendly GIS, focused on near real-time data visualization, for use in avalanche decision making by practitioners with minimal GIS experience. The user interface framework code was written in Python; the resulting software is a point-and-click, window-based product. The software can ingest multiple point clouds from TLS, photogrammetry, or any mixture of remotely sensed products. Point clouds may be pre-aligned (e.g., the Riegl workflow described in Section 2.2.2), or an Iterative Closest Point (ICP) algorithm can be run within the software to achieve alignment, depending on required accuracy and user-preference. Once aligned, the underlying algorithms delineate cliffs and vegetation to be excluded, then implement depth calculations from the snow surface to the base or any intermediate layer for which data is available. The visualization component allows the user to navigate around the scan, zoom in on regions, and select features. Users can select specific data to be displayed, such as coloring the scan by snow depth (e.g., a continuous gradient from red for deep snow to white for shallow). The back-end of the software system is designed to allow future extensions of capability and integration with new algorithms and analysis components. A more comprehensive overview of the software platform, including the annotated code and a user-manual, is provided in the supplemental material of this report.

---

date. NAD83(CSRS) epoch 2022.1 is a particular realization of the NAD83(CSRS) datum. The EPSG code is 8254.

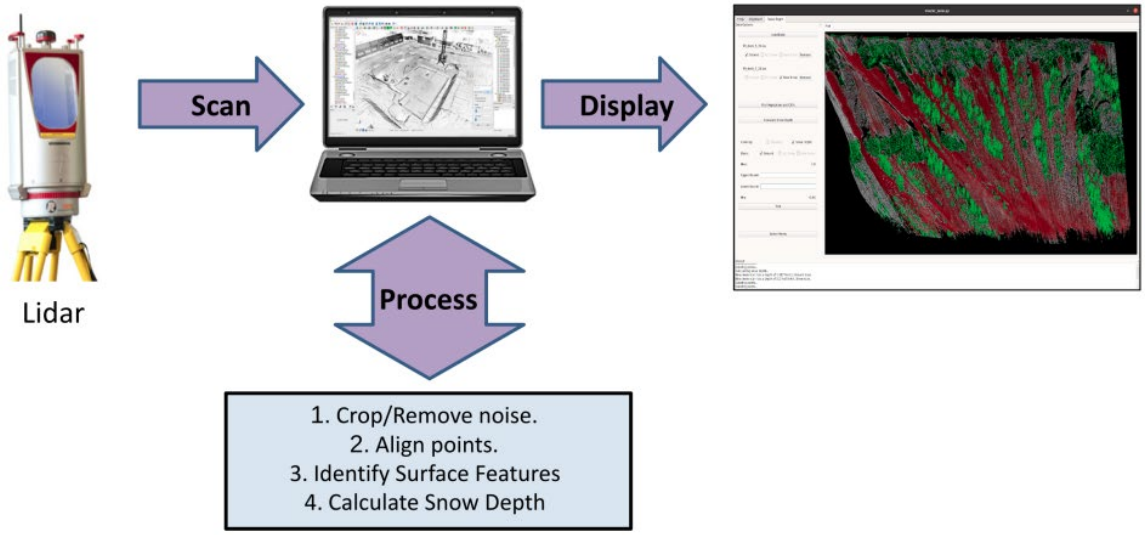

Figure 4. Diagram of general data collection and analysis workflow.

2.5 Laboratory Analyses

2.5.1 Lidar for Effective Grain Size and Density Mapping

In the cryosphere, lidar has almost exclusively been used as a spatial data tool for high-resolution snow depth mapping, as discussed above. However, lidar has the potential to be an ideal instrument for measuring NIR reflectance and subsequent estimation of snow surface properties. Most commercial lidars operate by emitting rapid pulses of light and record both the relative strength of backscattered signal after reflecting off a target, known as the return intensity, as well as the target's range. Each data point, or "return", has spatial coordinates (X, Y and Z) and a return intensity. Thus, lidar generates both a spatial and a radiometric data product. Furthermore, many lidar units operate at a NIR wavelength of 1064 nm, ideal for snow measurements. In the NIR spectral region, snow reflectance is determined by the effective grain size of the snow surface, a parameter essentially synonymous with the surface area-to-volume ratio (SSA) of the snow microstructure. For decades, NIR measurements have been used to estimate SSA, though the accuracy of using lidar in this manner has not been thoroughly evaluated; lidar is an optically unique case of bidirectional reflectance that requires careful examination. To address this knowledge gap, we conducted a laboratory reflectance study to determine how lidar reflectance varies with snow microstructure, specifically SSA and density. Success would lay the foundation for lidar-derived, spatially continuous maps of SSA and density to use in avalanche decision making alongside snow depth.

Twenty-five snow samples were generated within Montana State University's Subzero Research Laboratory (SRL). Snow used in testing was produced in the SRL's snowmaking apparatus. Differing grain habits were achieved by allowing bulk snow productions to undergo isothermal metamorphism at several subzero temperatures for various durations, essentially altering the initial conditions of microstructural grain habit amongst samples. Snow grains were then sieved through differing mesh sizes to further achieve disparate microstructures. Snow samples were prepared to be microstructurally homogeneous, both laterally across the sample width and vertically over sample depth. The physical properties of samples were characterized, as summarized in Table 1. Micro-CT was performed on a representative subset of each sample using a Bruker SkyScan 1173 housed in a -10° C chamber within the SRL, from which sample

SSA and snow density were calculated. Though samples were produced to be microstructurally homogeneous, 3D reconstructions from micro-CT data focused on the top 2 cm of samples to exclude optically inactive areas. Hereafter, the measured snow density in this 2 cm surface layer will be referred to as $\rho_{Surface}$.

Table 1. Physical snow sample characteristics organized by grain habit and listed in order of increasing grain size. The "C" along the sieve size of S25 implies that the sample was manually compressed to increase density.

Sample #	Grain Habit	Sieve Size (mm)	SSA (mm^{-1})	Micro-CT r_e (μm)	$\rho_{Surface}$ (kg m^{-3})	Total Porosity (%)
S1	PP	2.5	32.22	93	44	95.20
S2	PP	6.0	31.83	94	29	96.84
S3	PP	3.5	31.13	96	66	92.80
S4	PP	2.5	29.68	101	17	98.15
S5	PP	1.5	28.87	103	23	97.49
S6	PP	1.0	27.26	110	111	87.90
S7	PP	2.5	19.98	150	289	68.48
S8	DF	1.0	31.13	96	142	84.51
S9	DF	2.5	29.01	103	126	86.26
S10	DF	1.5	26.55	113	42	95.42
S11	DF	1.0	21.85	137	257	71.97
S12	DF	0.8	21.44	140	182	80.15
S13	DF	1.0	19.68	152	295	67.83
S14	DF	2.5	17.49	172	393	57.14
S15	DF	1.5	14.20	211	425	53.65
S16	RG	2.5	17.22	174	229	75.03
S17	RG	1.0	17.09	176	273	70.23
S18	RG	1.0	15.49	194	413	54.96
S19	RG	1.0	13.52	222	526	42.64
S20	RG	1.0	12.88	233	425	53.65
S21	RG	1.5	11.76	255	453	50.60
S22	RG	1.0	11.53	260	558	39.15
S23	RG	2.5	9.97	301	553	39.69
S24	RG	1.5	8.75	343	613	33.15
S25	RG	1.5C	6.73	446	679	25.95

Each sample was scanned with the VZ-6000 in a -3° C cold chamber. Scan durations were approximately 1 minute, with resulting point clouds generally containing about 5000 return points. Distance between the scanner and samples was 4.5 m, while incident beam diameter was 15.54 mm. A Lambertian reflectance standard with an albedo of 36% at 1064 nm was used to convert return power to bidirectional reflectance factor (*R*) for each individual point in the clouds. Examples of the resulting point cloud reflectance distributions are illustrated in Figure 5. Micro-CT scanning was conducted immediately after lidar data acquisition. Reflectance was related to SSA using the radiative transfer SNICAR (SNow, ICe, and Aerosol Radiative) model, while statistical analyses were used to calculate near-surface density as a function of reflectance.

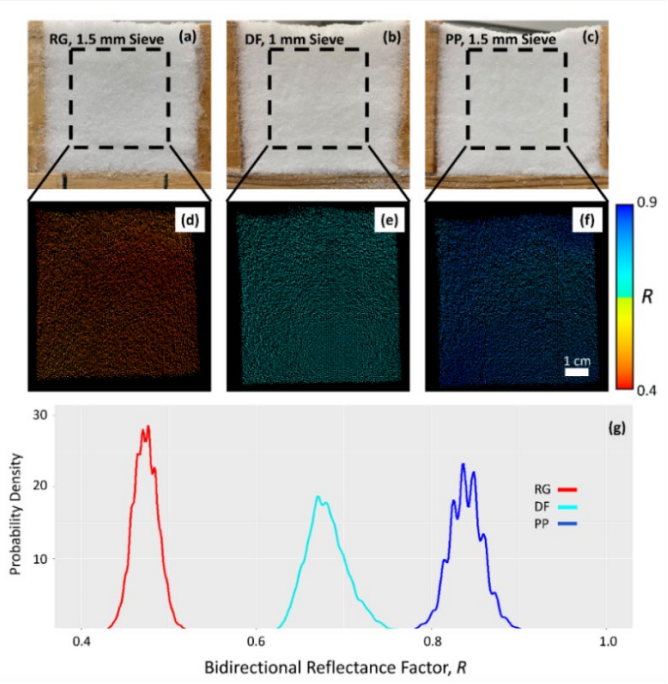

Figure 5. Visible imagery from three snow samples of differing microstructure (a – c), corresponding point clouds colored by bidirectional reflectance factor at 1064 nm (d – f), and a density plot of *R* distributions (g). The samples pictured are S5, S11, and S25.

2.5.2 Hyperspectral Imagery for Surface Hoar Mapping

Our 2nd laboratory objective was to adequately map surface hoar prior to burial using remote sensing instrumentation (Figure 6). The formation and disappearance of surface hoar are highly variable in space and time, and difficult to predict due to complex distributions of precipitation, wind, radiation and vegetation encountered in polar and mountainous environments. Further, the spatial distribution of surface hoar formation can vary on a sub-slope scale; temporally it can be promptly destroyed by environmental influences, or it can persist for weeks. Therefore, the detection of surface hoar presents itself as an ideal phenomenon for remote sensing. Success would provide forecasters with high-resolution observations of a prominent weak layer that frequently produces large avalanches, particularly as remote sensors and unmanned aerial vehicles become more cost-effective.

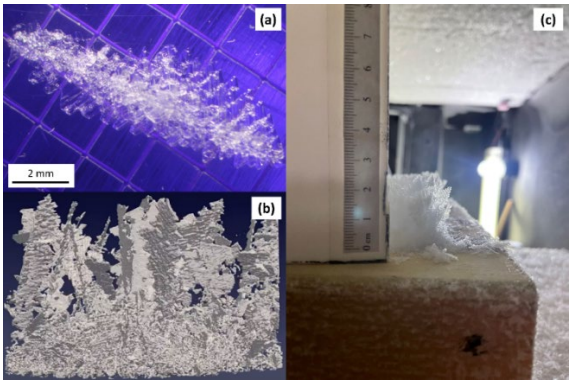

Figure 6. Laboratory-grown surface hoar crystals on a grain card (a), in a 3D reconstruction (b), and in profile (c).

Given that snow reflectance in the NIR is sensitive to snow microstructure (as described in Section 2.5.1), it is possible that downward-looking NIR measurements could be used to locate and delineate surface hoar prior to burial. Unfortunately, previous studies attempting this feat found that surface hoar crystals tend to produce moderate reflectance signatures relative to other grain shapes, making them difficult to discern from less-concerning snow structures based on NIR reflectance magnitude. Here, we hypothesize that the presence of surface hoar will coincide with a quantifiable increase in localized reflectance variance, termed NIR "texture", due to variable ice absorption. Texture is an underutilized parameter that quantifies optical roughness.

To examine the potential of surface hoar mapping with NIR remote sensing, we performed another laboratory experiment. Fourteen snow samples of disparate grain habits and microstructure (including surface hoar) were produced following Section 2.5.1. Samples were once again characterized using micro-CT. Furthermore, samples were not only scanned with the VZ-6000 lidar unit, but also with a Resonon Inc. Pika NIR-320 hyperspectral imager. Leveraging hyperspectral imagery allows for enhanced spectral resolution relative to lidar and builds on previous studies attempting to locate surface hoar with spectral data. The imager has a spectral resolution of 4.9 nm, measuring 164 bands across the NIR region from 900–1700 nm. The imager constructs a 2D image containing the full spectrum in each pixel by collecting the image line by line, known commonly as a "push broom" or "line" scanner. Thus, to collect an image, the camera needs to be moving (translating or rotating) relative to the scene, or the scene needs to be moving relative to the imager. In the laboratory, a linear scanning stage was used to move the sample beneath the sensor (Figure 7). Resulting images were processed in Resonon's proprietary Spectronon software.

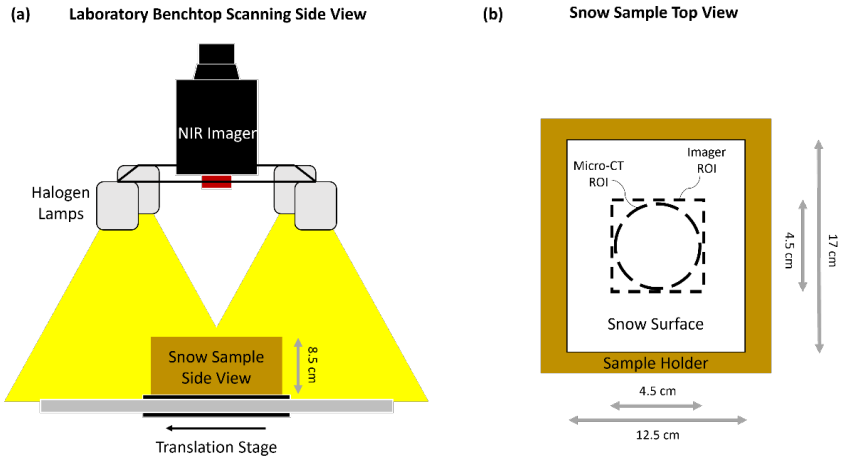

Figure 7. A schematic of the laboratory setup. A profile view of the imager apparatus (a) is shown beside a plan view of the snow sample holder and relevant ROIs (b).

To assess NIR texture, a simple moving window analysis was performed to convert hyperspectral and lidar-produced maps of reflectance to local standard deviation, σ_A, and local first derivative, $f'(A_b)$, both texture metrics. This process is demonstrated in Figure 8. Resulting distributions for each parameter were evaluated statistically across samples and visualized with a boxplot analysis. To produce classified maps of surface hoar extent, we investigated optimal threshold values of σ_A and $f'(A_b)$ to delineate surface hoar from other snow surface types on a per-pixel basis. Therefore, distributions (across all pixels) of σ_A and $f'(A_b)$ were examined between snow samples. Values where the probability density functions of the surface hoar sample and the next closest snow sample were determined to be the optimal thresholds for each parameter, termed $\sigma_{A,ctl}$ and $f'(A_b)_{ctl}$. These threshold values were used to perform binary classification of pixels using a simple two-tier classification tree. The classification algorithm was

run on all samples and accuracy assessed as the percentage of pixels correctly classified for each sample.

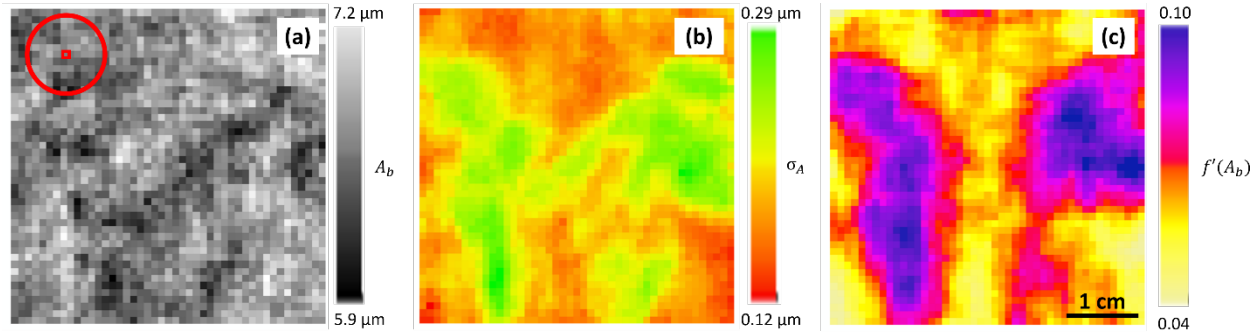

Figure 8. A moving window analysis was performed on an initial map of NIR reflectance (a) yielding grids of localized standard deviation (b) and first derivative (c).

3. Results

3.1 TLS Depth Mapping

Lidar-produced snow depth maps from the TLS were generally found to be in good agreement with field measurements, consistent with previous literature. It was found that, particularly when using tie point reflectors, lidar scans could be quickly acquired, aligned, and differenced to produce accurate depth maps at high spatial resolution. An example data product is depicted in Figure 9. General trends are apparent, such as heightened accumulation in gullies and minimal snow on cliff features. Furthermore, large deviations in depth across short spatial scales were captured (inset region). Adequate depth maps could be produced using the MSA workflow in the absence of tie points, although considerably more user processing was required to achieve comparable accuracy. When compared to manual depth observations at Bridger Bowl, the average error was found to be 16.5 cm with a low bias. That is, lidar-based depth calculations tended to underestimate actual snow depth. In the case of the Bridger Bowl test site, this was because of tall grass in the “snow-off” scan causing a slight, erroneous upward offset in the ground DEM, highlighting the benefit of acquiring ground scans in late autumn. This bias was found to be consistent across a large range of snow depths, as opposed to varying as a ratio of snow depth, and thus absolute error did not increase with depth.

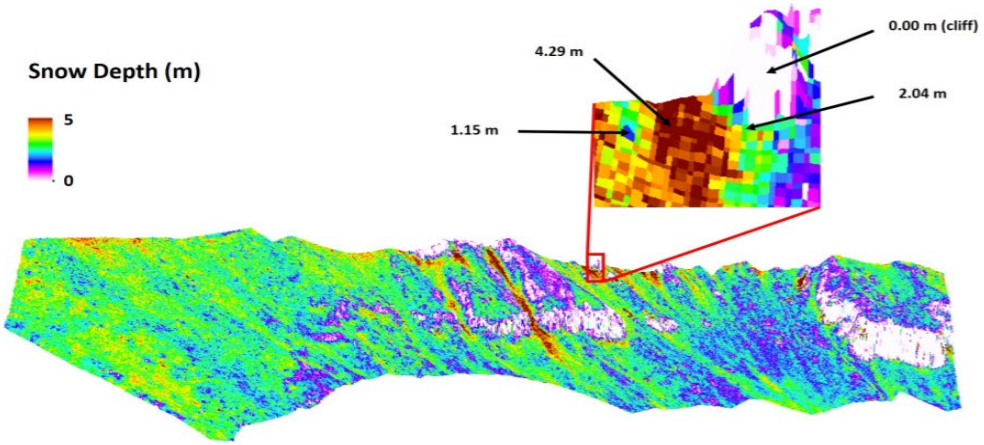

Figure 9. Snow depth map from the ridge leading to Pioneer Mountain at the Yellowstone Club.

Additional accuracy assessment points were provided by the photogrammetry GCPs, three of which happened to overlap with the snow-on lidar DEM at Glory Bowl. The mean offset between the lidar DEM and these GCPs was -12 cm, comparable to the magnitude and direction of bias observed at Bridger Bowl. Presumably this was also due to long grass in the ground (snow-off) scan. It's possible that, once identifying the grass-based offset for a given ground DEM, that a systematic translation could be used to correct this in subsequent depth map differencing, although this was not thoroughly explored here.

3.2 TLS – UAV Photogrammetry Comparison

Section 3.2.1 provides insight into the resulting orthomaps, DEMs and accuracy for the Westcamp site on Stevens Pass. The orthomaps and DEMs for Old Faihtful, Glorybowl and Yellowstone Club are provided in Appendix 5. Section 3.2.2 provides an assessment of the vertical accuracy of the UAV-based digital elevation models as compared to those of the TLS.

3.3 UAV Photogrammetry Performance

Figure 10 shows the UAV-based orthomosaic and DEM of Westcamp. The UAV-based orthomosaic and digital elevation model (DEM) show fine scale structure along the elevation gradient of the Westcamp site. The DEM is combined with a hillshade map to elucidate the relief. Both the orthomosaic and the DEM show traces of snow runout in the gully.

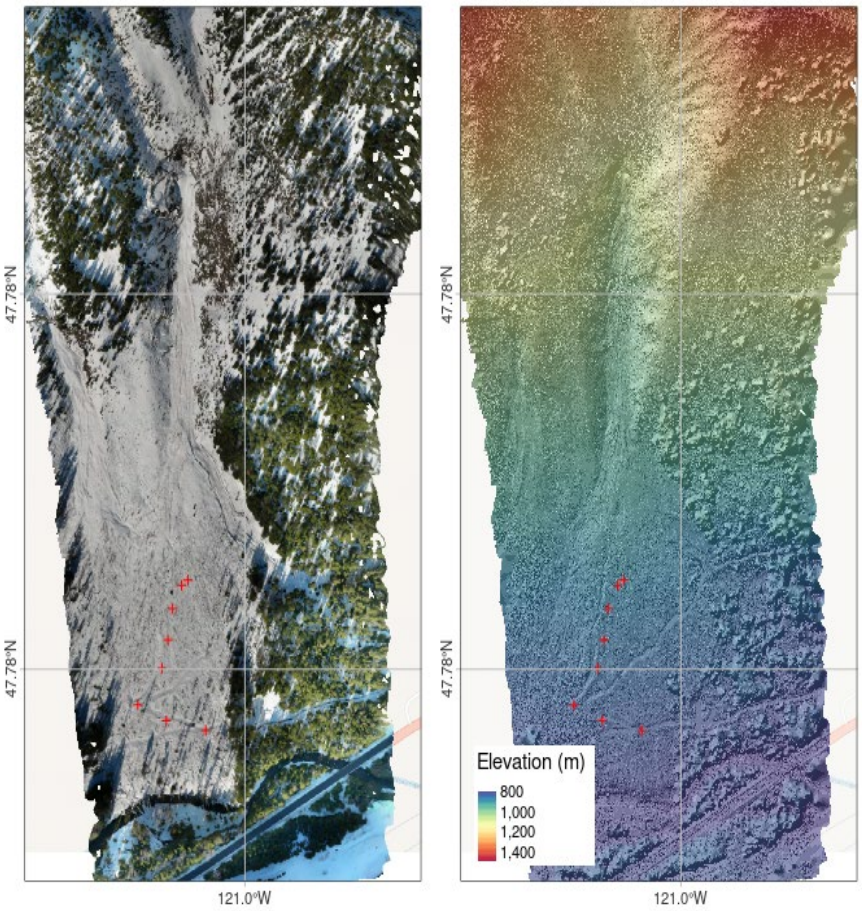

Figure 10. Westcamp orthomosaic (left) and DEM (right) with GCPs in red.

Figure 11 shows the spatial match between the orthomosaic of Westcamp and the eight independently measured ground control points (GCPs). It shows that the horizontal accuracy is high as the difference between the centers of the GCPs in the orthomosaic and the GNSS x-y measurement is not more than a few cm.

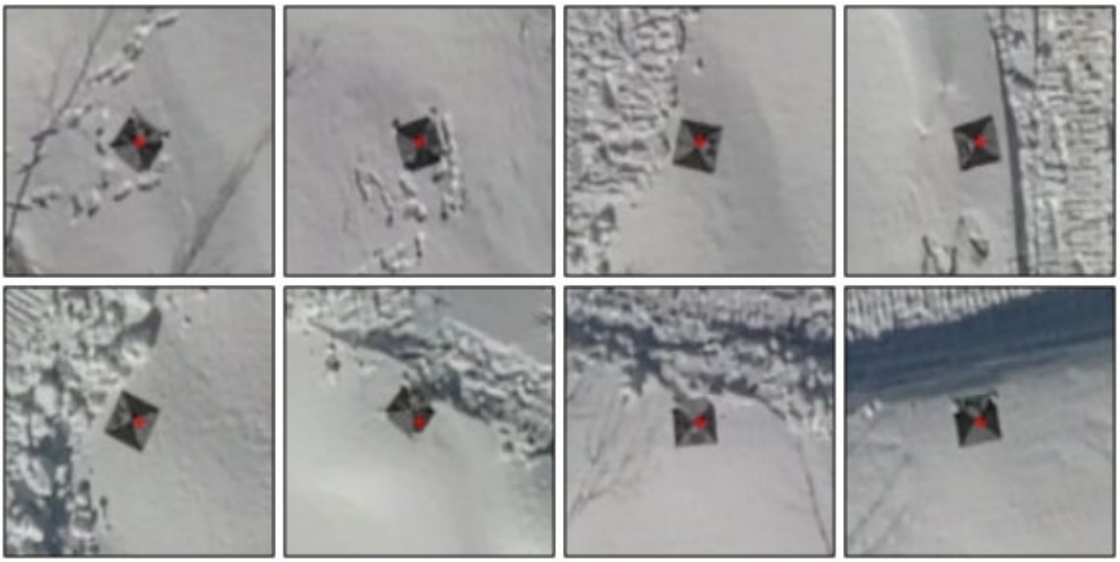

Figure 11. Detail of GCPs at Westcamp.

The overall correspondence between elevation from the DEM and independently measured elevation of the GCPs is illustrated in Figure 12. The vertical bias, i.e. the mean difference between the GCP elevation and the DEM elevation is -10.48 cm. The error (root mean square error, after accounting for the bias) is 5.16 cm which means that the method is accurate to a level of 5 cm on average. However, the observation that there is bias of -10.48 cm makes clear that it is important to include fixed points in the terrain that can be used to compare and if necessary spatially adjust maps and data.

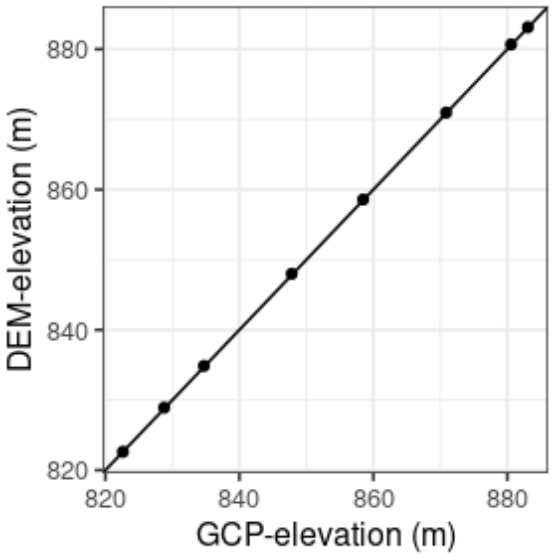

Figure 12. DEM-elevation vs independent GCP-elevation at Westcamp.

The overall correspondence between elevation from the DEM and independently measured by GNSS is illustrated in Table 2. It should be noted that in the case of Yellowstone Club (yc) real GCPs were not used; instead the location of reflectors that are used for processing the TLS measurements were used (see Figure 27 in Appendix). Unfortunately, the reflectors are not clearly visible in the orthomosaic and therefore the bias and error estimates are inaccurate. Although these data for Yellowstone Club are presented, we focus on the three sites where GCPs were visible as this provides a more realistic assessment (e.g., Figure 11).

The vertical bias, i.e. the mean difference between the GCP elevations and the DEM elevations varies between -56 and -10 cm. The error (rmse) varies between 3 and 8 cm and on average 5.3 cm.

site	ngcp	bias	rmse
westcamp	8	-0.10	0.05
oldfaithful	5	-0.35	0.03
glorybowl	8	-0.56	0.08
yc	3	-0.67	0.25

Table 2. Vertical accuracy of the UAV-based digital elevation models. Here, ngcp is number of ground control points, bias is mean difference of height measurements (m), and rmse is root mean square error (m).

3.3.1 Comparative Assessment

Given that both lidar and photogrammetric DEMs were of suitable accuracy, comparisons between products were also generally found to be accurate for snow depth retrieval estimates. The primary comparison was conducted at Glory Bowl (Teton Pass, WY). Initially, the mean offset between the lidar and photogrammetric DEM was about 40 cm (with the UAV DEM being 40 cm lower). This is consistent with the observed offsets between these DEMs and the GCPs (-12 cm for lidar and -56 cm for UAV). Once the UAV-based DEM was translated to account for the vertical offset with GCPs, the DEMs were in even better agreement, as depicted in Figure 13. Furthermore, in Figure 14, elevation values for the central transect (black line in Figure 13) are presented, as well as differences between lidar and UAV along the transect. Careful observations of these results, as well as juxtaposing workflows, have revealed several strengths and weaknesses of TLS lidar versus UAV photogrammetry.

Strengths of TLS Lidar

- Terrestrial unit can be operated in inclement weather
- As an active sensor, lidar can produce depth maps both under canopy and at night
- Lidar produces a radiometric data product (NIR reflectance) that can be used to calculate snow surface properties (Section 3.4)

Weaknesses of TLS Lidar

- Expensive (currently decreasing in cost, but requires a “buy-in” up front to use the technology)

- “Shadowing” from terrain results in blank regions in the point cloud and corresponding local miscalculations in the DEM (large spike in Figure 14), when using terrestrial systems
- NIR lasers may have eye-safety concerns (1064 nm is not eye safe, even though the beam is invisible to the naked eye)

Strengths of UAV Photogrammetry

- Drone-based, downward looking system eliminates terrain shadowing and provides a more comprehensive DEM, especially in open areas
- Reasonably cost-effective
- A coincident, high-resolution orthophoto image is also produced in addition to a DEM
- Easy to transport

Weaknesses of UAV Photogrammetry

- Inability to penetrate vegetation/canopy cover
- Drone system requires manageable weather conditions for flight
- Data can only be collected during the day and no NIR data are acquired

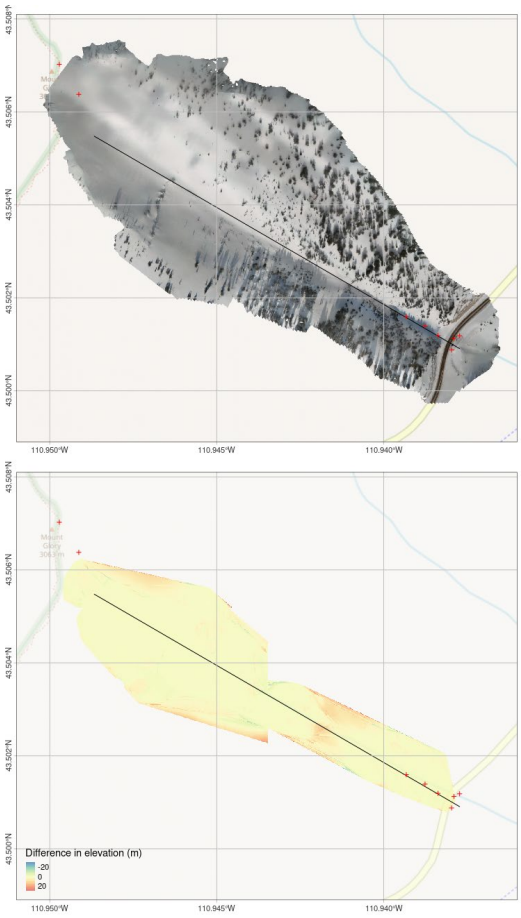

Figure 13. Glorybowl orthomosaic (top) and a map of the difference in DEM between photogrammetry and lidar (bottom). GCPs in red and transect in black line.

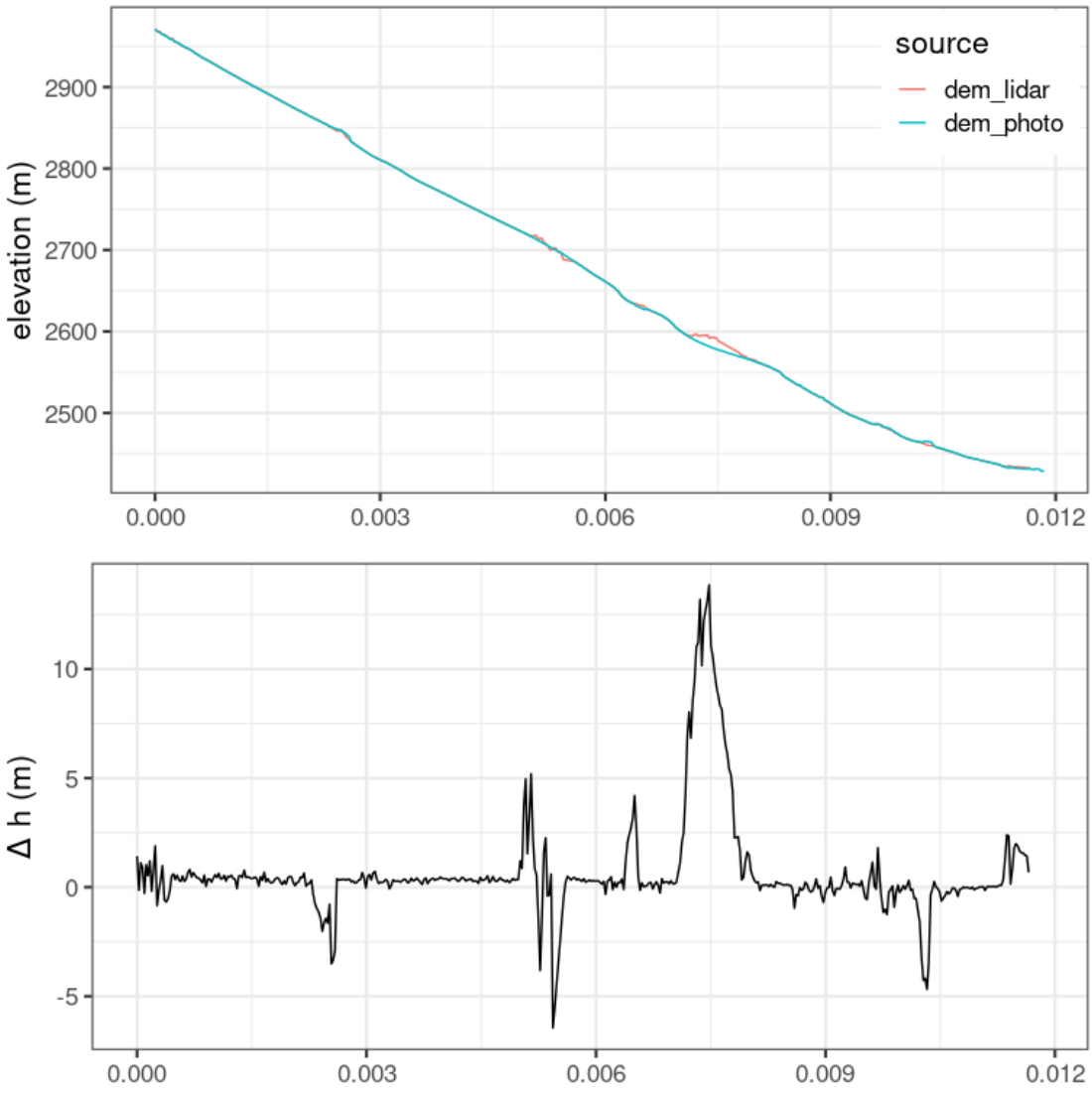

Figure 14. Elevation along the transect in Figure 13 (top), and differences between lidar and photogrammetry DEMs along the transect (bottom).

3.4 GIS Software Product

As introduced in Section 2, a GIS software product was created that allows for minimal user-inputs, aside from the obtained TLS point-clouds. An example of the resultant visualization is shown in Figure 15. Included in the supplementary material for this report is the annotated Python code, a detailed user manual, an overview document, and recorded video demonstration. Although further ground validation remains needed for various terrain types and locations, within our test-sites, the snow depth estimates were found to be accurate and within "tolerable" limits of error for avalanche forecasting purposes (+/- 10 cm), largely dependent on the snow-off scan used as the baseline elevation dataset and whether or not vegetation was present in the

scan and/or if it became more compressed under the snow load.

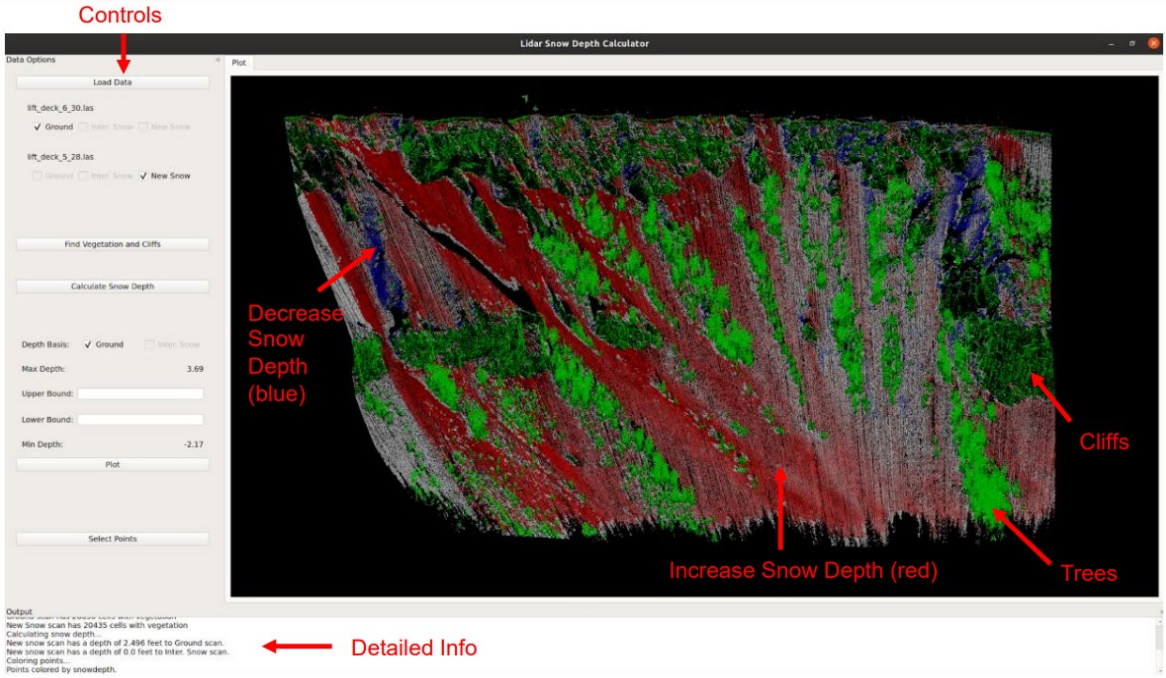

Figure 15. Example of visualization interface from the Yellowstone Club.

3.5 Laboratory Findings

3.5.1 Lidar for Effective Grain Size and Density Mapping

Estimates of effective grain size (and thus SSA) derived from lidar reflectance produced a mean error of 12.7% relative to micro-CT measurements. This was an excellent result that surpasses the accuracy of many other NIR instruments. Example maps and boxplots of effective grain size retrievals are compared to micro-CT observations in Figure 16. Furthermore, it was found that SSA and density were more closely associated than previous literature suggests (R^2 = 0.92). This allowed for simultaneous estimates of both SSA and near-surface snow density from NIR lidar reflectance measurements. Resulting density estimates produced a mean error of 47.1 kg m^{-3} (20.0%). This novel finding marks, to the best of our knowledge, the first instance of density estimation from optical data, and demonstrates the capacity of lidar as both a spatial and radiometric mapping device.

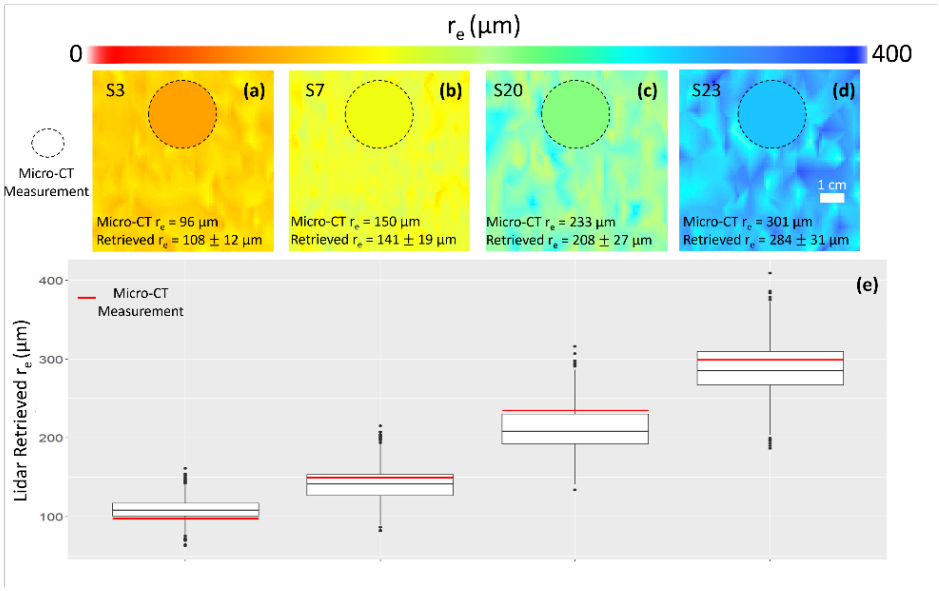

Figure 16. Maps of lidar retrieved effective grain size (r_e) for four samples with a range of r_e values (a – d), and an associated boxplot of sample distributions (e). Again, r_e is essentially synonymous with SSA. Dotted circles represent the micro-CT ROI, colored by micro-CT measured r_e.

3.5.2 Hyperspectral Imagery for Surface Hoar Mapping

Results of surface hoar mapping from hyperspectral imagery are presented here; classification via lidar efforts are ongoing. Significance test results verified our hypothesis; the mean values of both texture parameters, σ_A and f'(A_b), were found to be significantly higher in the surface hoar sample (SH) relative to all other samples ($p < 0.001$ in all cases). This distinction is apparent when observing the boxplots presented in Figure 17. For both parameters, the mean value of the next closest distribution (Sample 6, faceted crystals) was well beneath that of Sample SH. Thus, the pixel distributions of texture metrics for surface hoar were considerably larger than all other samples, and therefore easily discernible. This allowed for pixelwise delineation of surface hoar using a two-tiered classification tree analysis. The classification algorithm was run on all fourteen samples, and was near perfect at correctly refuting the presence of surface hoar when it is indeed absent. Further, the algorithm correctly identified surface hoar in 89.5% of pixels. Error in positive identification appeared to be mostly attributed to sporadic, small areas of misclassification rather than systemic error with a discernible pattern. Last, an accuracy assessment was performed on a brand-new sample split roughly 1:1 between rounded grains and surface hoar, with an overall accuracy of 82.8% (Figure 18).

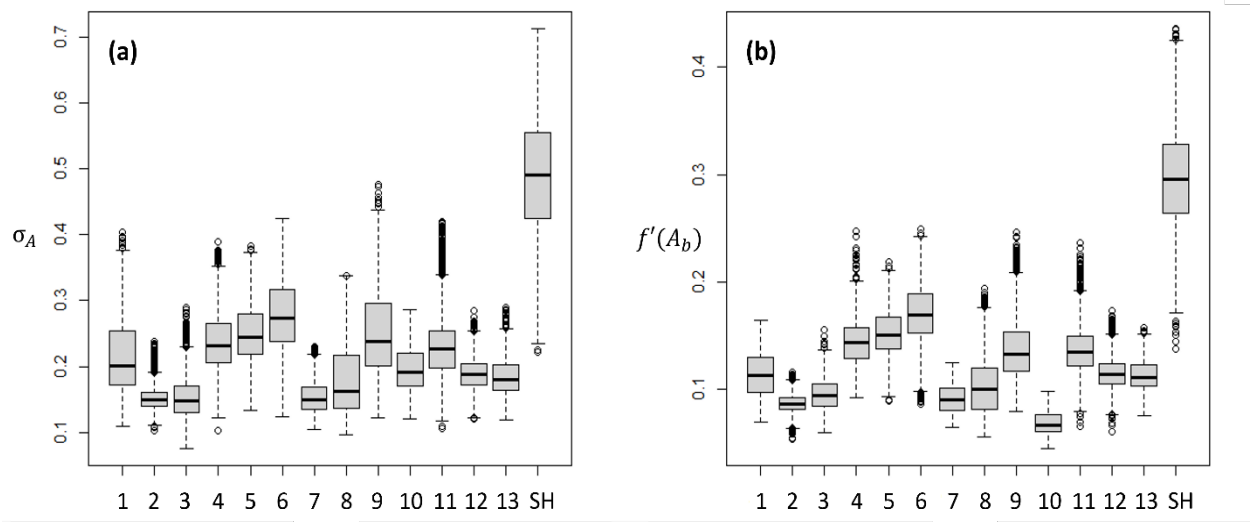

Figure 17. Boxplot analysis of texture parameter distributions.

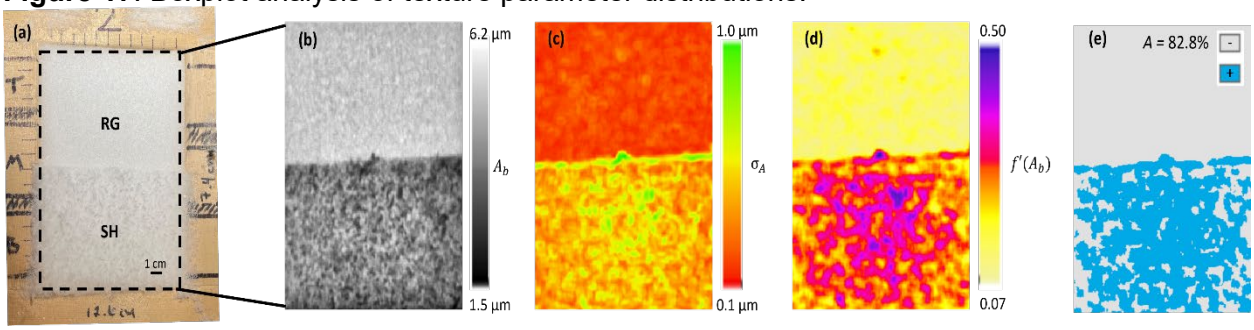

Figure 18. A visible image of a roughly 1:1 RG (top) to SH (bottom) sample (a) was analyzed with a hyperspectral imager to NIR reflectance (b). A moving window analysis was performed to produce maps of texture parameters (c and d), which were used in a classification workflow to create a binary map of surface hoar (e).

4. Conclusions

Our results can be generalized into three categories: field, software, and laboratory.

Field: We have further validated the use of TLS lidar and UAV photogrammetry for snow depth mapping, and demonstrated their interchangeable capacity. We have outlined best practices, as well as strengths and weaknesses of each method independently.

Software: We have created an open-source, user-friendly GIS software product capable of alignment, depth calculations, and interactive viewing, built specifically for avalanche practitioners. The back-end of the code was designed for further expansion based on laboratory findings, future applications, etc., and is compatible with any point cloud data, including those produced from both lidar and photogrammetry.

Laboratory: We have demonstrated the ability of lidar to map SSA with accuracy comparable to passive remote sensing techniques. Furthermore, we presented novel methods for mapping both density and the distribution of surface hoar.

Due in-part to the foundational work presented here, future forecasting operations will be able to use any combination of remote sensing systems to produce maps of terrain metrics, snow depth, and snow surface properties in real-time, as demonstrated in Figure 19.

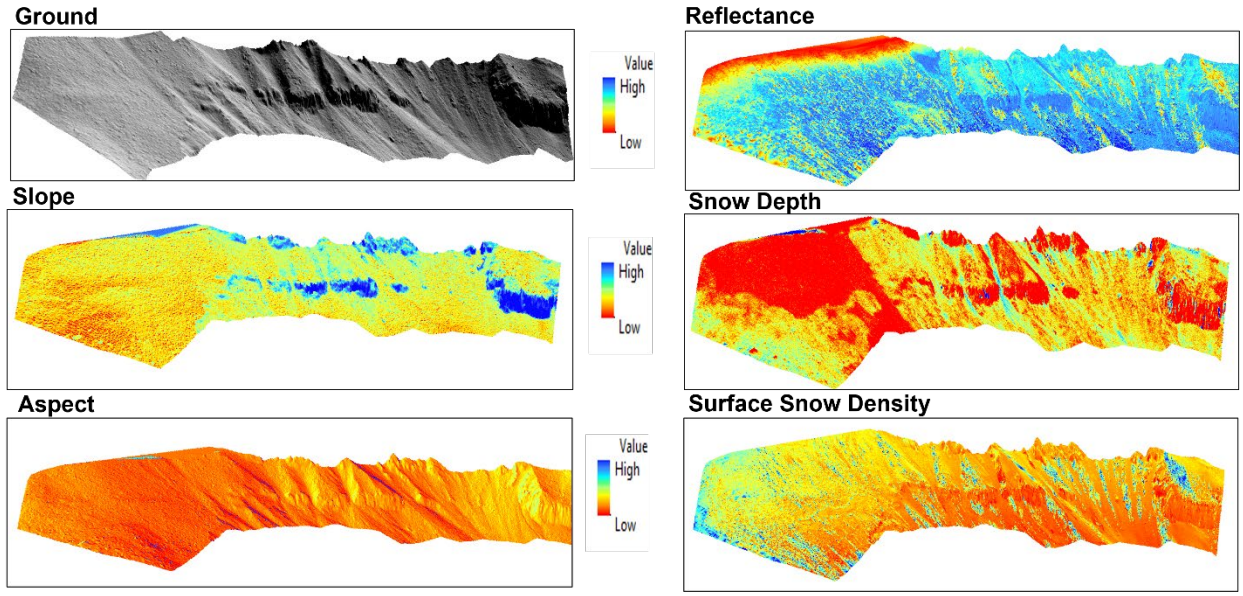

Figure 19. Coincident visualizations of terrain features and physical snowpack properties produced by TLS lidar. The area shown is the ridge leading to Pioneer Mountain at the Yellowstone Club.

5. Appendix – 1

5.1 Old Faithful

Figure 20 show the orthomosaic and the DEM for Old Faithful. The red crosses show the locations of the GCPs. Figure 21 shows the location of the GCPs and the markers in the field in detail. It shows that the distance between the GCPs and the marker in the orthomosaic is only a couple of cm at maximum.

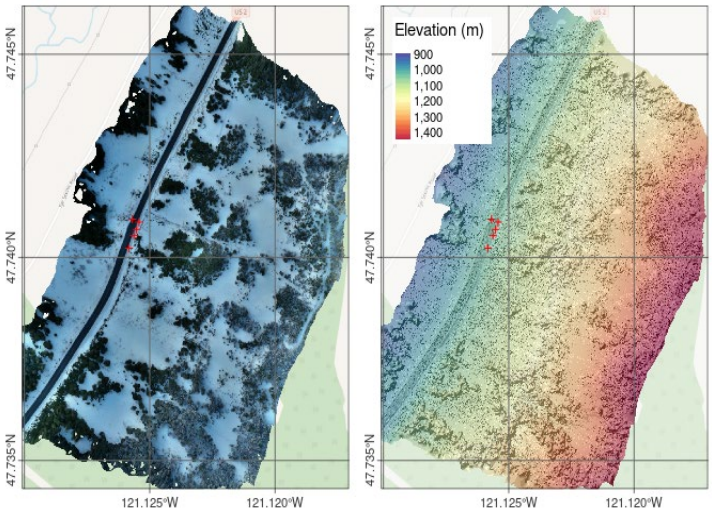

Figure 20. Old Faithful orthomosaic and digital elevation model (DEM) with GCPs in red.

Figure 21. Detail of GCPs at Old Faithful.

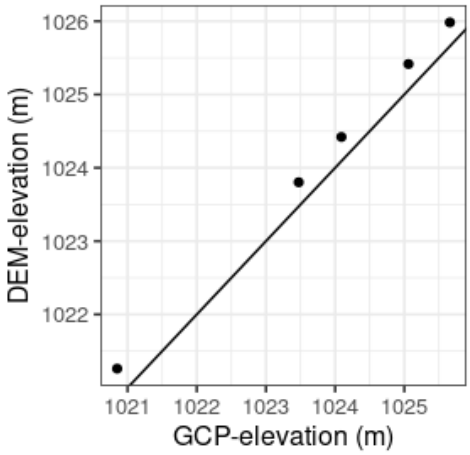

Figure 22. DEM-elevation vs independent GCP-elevation at Old Faithful.

5.2 Glory Bowl

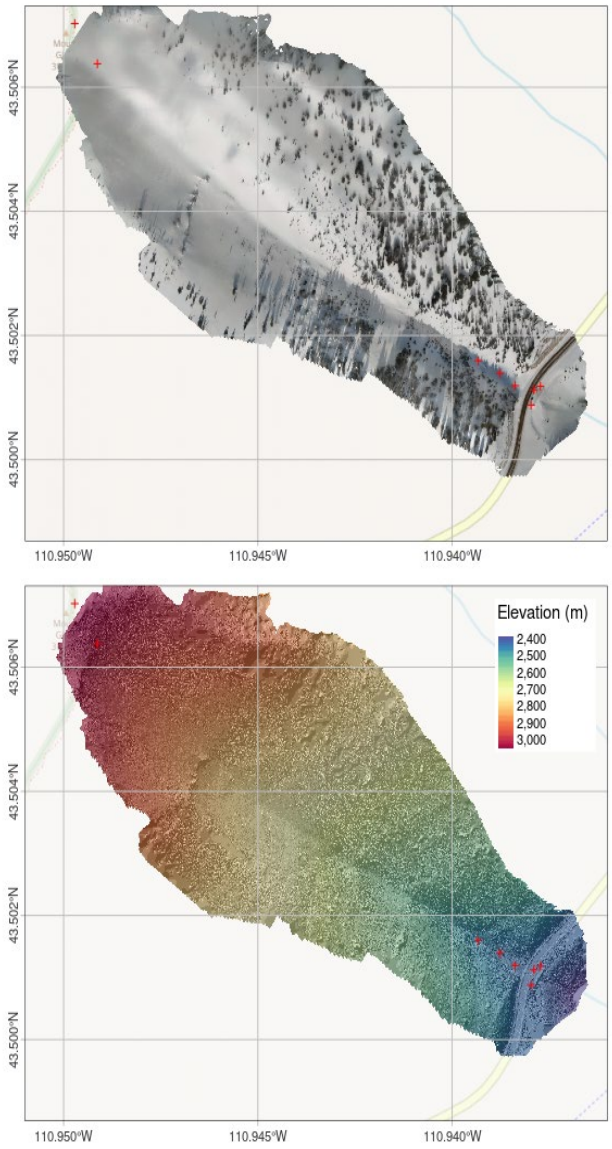

Figure 23. Glorybowl orthomosaic and digital elevation model (DEM) with GCPs in red.

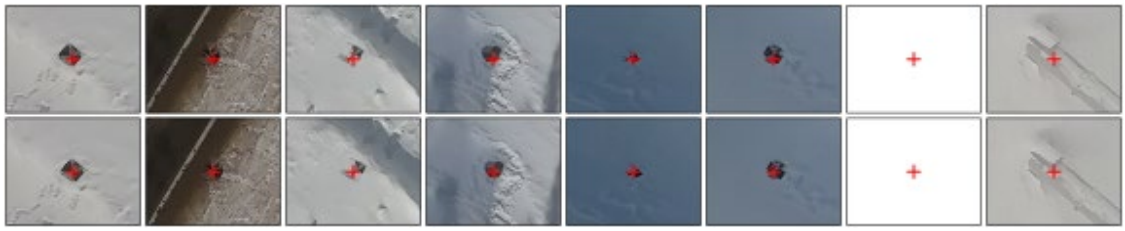

Figure 24. Detail of GCPs at Glorybowl before (top row) and after (bottom row) translation.

In the case of Glorybowl there was a small systematic shift in the vertical plane between the GCPs and the orthomosaic (Figure 24). The xy-shift values are found by visually matching the ortho with the gcps. This shift was accounted for before assessing the vertical accuracy.

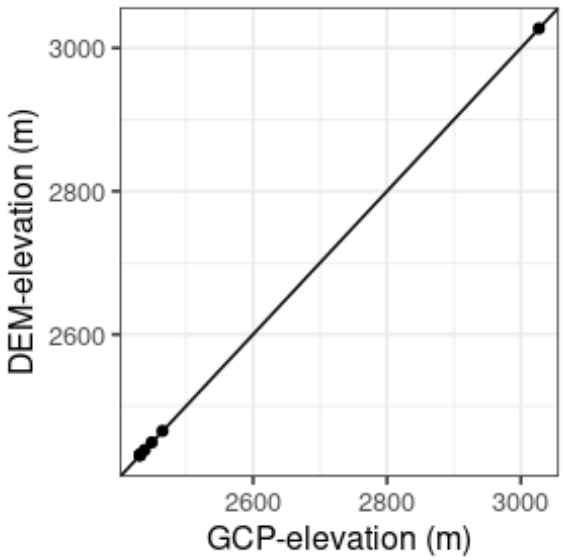

Figure 25. DEM-elevation vs independent GCP-elevation at Glorybowl.

The overall correspondence between elevation from the DEM and independently measured by GNSS is illustrated in Figure 25. The vertical bias, i.e. the mean difference between the GCP elevation and the DEM elevation is -56 cm. The error (rmse) is 8 cm.

5.3 Yellowstone Club

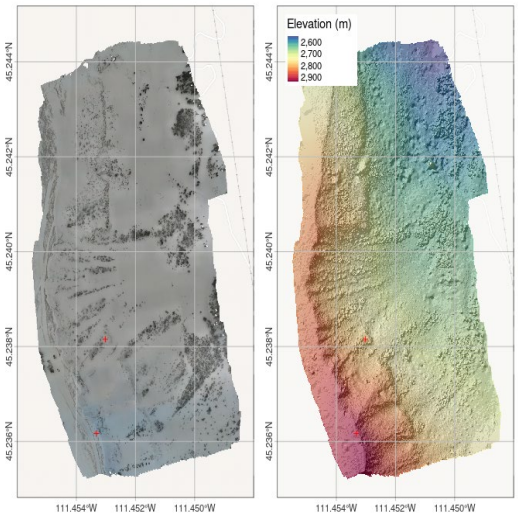

Figure 26. Yellowstone Club orthomosaic and digital elevation model (DEM) with GCPs in red.

Figure 27. Detail of reflector locations at Yellowstone Club.

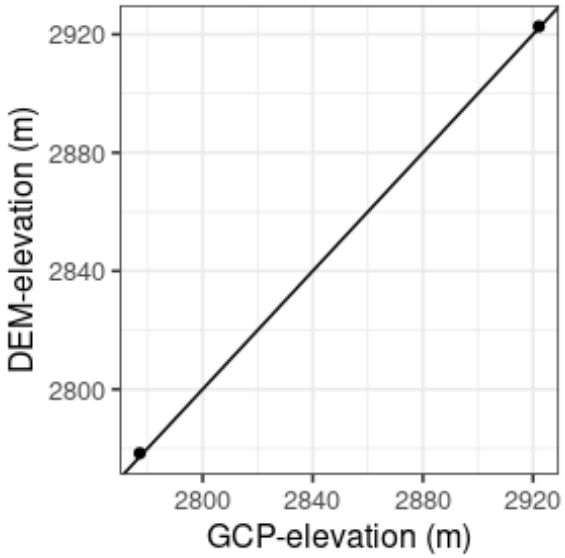

Figure 28. DEM-elevation vs independent GCP-elevation at Yellowstone Club. The reflectors are used as GCPs.